In situ observations of particles in jet aircraft exhausts and contrails for different sulfur-containing fuels

U. Schumann,[1] J. Ström,[2] R. Busen,[1] R. Baumann,[1] K. Gierens,[1] M. Krautstrunk,[1] F. P. Schröder,[2] and J. Stingl[1]

Abstract. The impact of sulfur oxides on particle formation and contrails is investigated in the exhaust plumes of a twin-engine jet aircraft. Different fuels were used with sulfur mass fractions of 170 and 5500 ppm in the fuel, one lower than average, the other above the specification limit of standard Jet-A1 fuel. During various phases of the same flight, the two engines burnt either high- or low-sulfur fuel or different fuels in the two engines. Besides visual, photographic, and video observations from close distance, in situ measurements were made within the plumes at plume ages of 20 to 30 s, at altitudes between 9 and 9.5 km, and temperatures between -49 and -55°C, when the visible contrail was about 2 km long. The data include particle number densities for particles larger than 7 nm, 18 nm, 120 nm, and 1 μm in diameter, together with wind, temperature and humidity measurements. The observations show visible and measurable differences between contrails caused by the different sulfur levels. At ambient temperatures 5 K below the threshold temperature for contrail onset, the plume became visible about 10 m after the engine exit for high sulfur content, but 15 m after the engine exit for low sulfur content. The higher sulfur emission caused a larger optical thickness of the contrail shortly after onset, with slightly brown-colored contrail when the Sun was behind the observer, and more contrast when viewed against the Sun. The high-sulfur contrail grew more quickly but also evaporated earlier than the low-sulfur contrail. At plume ages of about 20 s, each engine plume was diluted to an effective diameter of 20 m. The plumes contained many subvisible particles. Peak number densities were 30,000 cm^{-3} for particles of diameter above 7 nm and 15,000 cm^3 above 18 nm. The latter is a little larger than the estimated number of soot particles emitted. The high-sulfur plume shows more particles than the low-sulfur plume. The differences are about 25% for particles above 7 nm and about 50% above 18 nm. The results indicate that part of the fuel sulfur is converted to sulfuric acid which nucleates with water vapor heterogeneously on soot or nucleates acid droplets homogeneously which then coagulate partly with soot. During descent through the level of contrail onset, the high-sulfur contrail remained visible at slightly lower altitude (25 to 50 m) or higher temperature (0.2 to 0.4 K). At least for average to high sulfur contents, aircraft generate an invisible aerosol trail which enhances the background level of condensation nuclei, in particular in regions with dense air traffic at northern latitudes and near the tropopause.

1. Introduction

Contrails (condensation trails) from engine exhaust of high-flying aircraft may influence the climatological and chemical state of the atmosphere [*Schumann*, 1994; *World Meteorological Organization (WMO)*, 1995]. As first explained by *Schmidt* [1941] and *Appleman* [1953] using a thermodynamical equilibrium theory, contrails are expected to form in the engine exhaust plumes when isobaric mixing between the hot and humid exhaust gases and cold ambient air leads to a mixture reaching saturation with respect to water so that cloud droplets form which then

might freeze to form ice particles. For ambient humidity sufficiently below ice saturation, the contrails evaporate and remain short-lived while persistent contrails may form otherwise. In order to reach water saturation in the plume, the ambient air temperature must be below a certain threshold temperature which depends on pressure, ambient humidity, and the ratio of water vapor and heat emissions from the engines. Small changes in the threshold temperature can cause considerable changes in the altitude range where contrails form [*Miake-Lye et al.*, 1993]. The threshold temperature is larger than predicted by *Appleman* [1953] because only part of the combustion heat is emitted with the exhaust while a fraction η is converted into work to propel the aircraft, where η is the overall propulsion efficiency of the engine/aircraft combination [*Busen and Schumann*, 1995]. In order to form droplets when reaching small liquid supersaturation, the exhaust must contain sufficient cloud condensation nuclei (CCN). It is an open question how these CCN are formed.

Particle measurements in exhaust plumes [*Knollenberg*, 1972; *Baumgardner and Cooper*, 1994; *Fahey et al.*, 1995; *Gayet et al.*, 1996] show very large concentrations of particles which

---

[1]Deutsche Forschungsanstalt für Luft- und Raumfahrt (DLR), Institut für Physik der Atmosphäre, Oberpfaffenhofen, Germany.

[2]Department of Meteorology, Stockholm University, Stockholm, Sweden.

cannot be explained by background aerosol. Possible alternative sources are soot [*Pitchford et al.*, 1991; *Hagen et al.*, 1992] and sulfur emissions [*Hofmann and Rosen*, 1978] from the engine exhaust, or combinations of both. These emissions may lead to an invisible aerosol trail [*Arnold et al.*, 1994].

Jet fuels contain sulfur with typical mass concentrations between 100 and 1000 ppm [*Busen and Schumann*, 1995] and maximum specification limit of 3000 ppm [*American Society for Testing and Materials (ASTM)*, 1994]. In burning the fuel with air, jet aircraft emit sulfurous gases, mostly SO_2, formed by oxidation of the fuel sulfur during combustion [*Frenzel and Arnold*, 1994]. Measurements [*Reiner and Arnold*, 1993] and model computations [*Miake-Lye et al.*, 1994; *Kärcher et al.*, 1995] indicate that 0.4 to 0.7% of the SO_2 is converted to sulfuric acid in the young exhaust plume. Hence the CCN for contrail formation may originate from binary nucleation of sulfuric acid with water [*Mirabel and Katz*, 1974; *Hofmann and Rosen*, 1978]. Solution droplets may freeze and grow as ice particles [*Heymsfield and Sabin*, 1989] even before reaching liquid water saturation. However, model results [*Kärcher et al.*, 1995] show that homogeneous nucleation of H_2SO_4/H_2O from the gas phase leads to too small droplets which do not freeze quick enough and cannot explain the formation of a visible contrail unless the liquid supersaturation in the exhaust plume becomes large. Hence one has also to consider heterogeneous nucleation of sulfuric acid with water on the surface of soot particles emitted by jet engines [*Turco et al.*, 1980; *Miake-Lye et al.*, 1994].

Soot usually consists of more than 90% carbon with properties depending strongly on the combustion process [*Haynes and Wagner*, 1981]. Typically, jet engines emit 0.1 to 1 g of soot per kilogram of fuel [*Turco et al.*, 1980; *U.S. Environmental Protection Agency (EPA)*, 1985], with peak diameters of 30 to 100 nm [*Hagen et al.*, 1992]. Pure carbon particles are hydrophobic and form condensation nuclei only for large supersaturation. Aerosol resulting from combustion of aviation fuel usually contains only a low fraction of CCN [*Hallett et al.*, 1990; *Pitchford et al.*, 1991]. However, soot particles coated with sulfuric acid provide a source for CCN [*Parungo et al.*, 1992] and carbon particles exposed to H_2SO_4 hydrate under subsaturation conditions [*Wyslouzil et al.*, 1994]. Soot from diesel combustion in diffusion flames (without reaching water saturation) forms CCN for smaller soot radii when sulfur is added to the fuel [*Lammel and Novakov*, 1995]. Droplets formed from soot may undergo immersion freezing at temperatures between -24° and -34°C, and homogeneous freezing at lower temperatures [*DeMott*, 1990]. A recent model study showed that a substantial fraction of soot particles in exhaust plumes may get converted into acid aerosols by heterogeneous nucleation [*Zhao and Turco*, 1995]. It appears plausible that the fraction of soot particles activated this way to form CCN and visible contrail particles increases with the sulfur content in the fuel.

Hence impact of sulfur emissions on particle formation is expected but experimental evidence for such impact in aircraft exhaust plumes is missing. In a recent experiment, *Busen and Schumann* [1995] found no visible difference between the contrails of two engines burning different fuels, one with low (2 ppm) sulfur content, the other with average (250 ppm) sulfur content. This paper presents observations from a repetition of that experiment in which the aircraft during one flight burnt again different fuels in the two engines but with higher sulfur contents of 170 and 5500 ppm, respectively. In addition to measurements of the thermodynamic state of the atmosphere and turbulence in the exhaust plume, measurements of particle num-

ber densities and size distributions were conducted in the plume at a distance of 3 to 5 km behind the aircraft, under conditions of short-lived contrails.

2. Experimental Details

The experiment is performed using two aircraft. The contrails which we observe are generated, as in the previous study [*Busen and Schumann*, 1995], with the ATTAS (Advanced Technologies Testing Aircraft System) of DLR (Deutsche Forschungsanstalt für Luft- und Raumfahrt), a moderate size twin-engine jet aircraft of type VFW 614, equipped with two Rolls Royce/SNECMA M45H Mk501 turbofan engines as described in *JANE* [1976, pp. 98, 704] and *JANE* [1980, pp. 723 and 724]. The aircraft has a wing span of 21.5 m, an overall length of 20.6 m, a maximum speed of Mach 0.65, and a ceiling of about 9500 m. The two engines are mounted on overwing pylons. The engines have a bypass ratio of 3:1 and produce 32.4 kN takeoff thrust. They generate relatively large amounts of soot (about 5 times more than most modern engines). Observations were performed with the Falcon research aircraft of the DLR, also a twin-engine jet aircraft (Dassault Mystere 20) [*JANE*, 1975, pp. 63-65], which may follow the ATTAS at all altitudes and speeds.

The ATTAS engines can be supplied with fuel from either the left or the right tank, by switching valves in its fuel system. This facility is used to perform measurements during the same flight in various "phases," with low sulfur fuel for the left and high sulfur fuel for the right engine (LH), both engines with high (HH), and both engines with low (LL) sulfur content fuel. The ATTAS wing tanks have a capacity of 3115 L, each. The left wing tank was filled with standard Jet-A1 fuel. The right tank was filled with the same fuel together with 60 kg of an additive (dibutylsulfide) containing 22% sulfur mass. The additive was added in six portions during tank filling. The melting, boiling, and flame point temperatures of the additive are very similar to those of Jet-A1, but its density is about 5% larger. Fuel analysis of samples taken according to *ASTM* [1994] standards after the flight, see Table 1, revealed that the fuel with the sulfur additive satisfies all requirements for Jet-A1 fuel except for the high sulfur content. Samples (5 L) taken before the flight showed 180 ppm for the left wing tank but a much higher sulfur content (48100 ppm) for the right wing tank because of sedimenting of the heavier additive in the 36 hours between filling and sampling. The measured sulfur content of the sample taken after the flight is very close to that computable from the known sulfur content of the original fuel and the amount of sulfur added (see Table 1). The same is true for the hydrogen content of the mixture within the accuracy of such analysis ($\pm 0.16\%$, according to ASTM D 3343, pp. 435). Thus we can assume that the additive has been well mixed with the fuel shortly after takeoff. The contrail formation depends on the ratio of specific combustion heat and the emission index (EI) for water, Q/EI_{H_2O}, which differs by only 0.6% between the two fuels.

Table 2 lists the instruments used on the Falcon. The meteorological instrumentation [*Bögel and Baumann*, 1991; *Schumann et al.*, 1995] includes two instruments to detect slow and quick variations in relative humidity (RH) [*Ström et al.*, 1994]. The absolute accuracy of the HUMICAP sensor is about $\pm 5\%$ relative humidity at 50% RH, decreasing at lower and increasing at higher RH. The sum of errors of the humidity and temperature sensors implies an upper error bound of $\pm 10\%$ added RH for our measurements at -53°C, 267 hPa, and 50% RH. Four instruments are used to count and size the aerosol. Two of the instruments

Table 1. Fuel Parameters for Left and Right Engines

Parameter	Left	Right	Limit
Sulfur content after flight, ppm	166	5400	3000
Computed sulfur content, ppm		5466	
Hydrogen content, mass %	13.71	13.64	
Computed hydrogen content, mass %		13.68	
Computed EI_{H_2O}, kg kg^{-1}	1.225	1.215	
Density at 15°C, kg m^{-3}	808.2	795.0	775 to 840
Anilin point, °C	58.8	58.2	-
Specific heat of combustion Q, MJ kg^{-1}	43.20	43.11	42.5
Aromatics content, vol %	17.7	17.5	22
Initial boiling point, °C	174	167	
10% distillation, °C	189	175	205
20% distillation, °C	193	179	
50% distillation, °C	204	188	
90% distillation, °C	228	232	
Boiling end point, °C	256	267	300
Residuum, vol %	0.9	0.9	1.5
Loss, vol %	0.1	0.1	1.5
Olefins content, vol %	0.5	0.7	5
Naphthalenes content, vol %	-	0.9	3
Smoke point, mm	23	24	19

The data are from samples taken after the flight, except for the last three entries which are from samples taken before the flight from the same fuel storage tank, without and with the sulfur additive. The limits refer to American Society for Testing and Materials specifications for Jet-A1 fuel.

were modified TSI 3760 CPCs (condensation particle counter) [*Noone and Hansson*, 1990; *Zhang and Liu*, 1991], the two other instruments are optical particle counters, a passive cavity aerosol spectrometer probe (PCASP), and a forward scattering spectrometer probe (FSSP) [*Dye and Baumgardner*, 1984]. The CPCs count optically the number of particles which grow to about 1 µm after supersaturation with butanol and cooling by a condenser. The PCASP and the FSSP count and size particles in different size ranges by detecting the amount of light which is scattered from particles when passing through a laser beam. The air inlet for the CPCs and the PCASP collects particles smaller than 1 µm. The CPCs count the number of particles larger than 7 nm and 18 nm of effectively dry aerosol, including soot and sulfuric acid droplets with low water content. The PCASP covers the size range between 0.1 and 3.5 µm which is divided into 32 size classes. Due to the design of the aerosol inlet and an erro-

neous first size bin, the integral number concentration as measured by the PCASP represents particles between 120 nm and about 1 µm diameter. The FSSP (type 100) mounted below the fuselage detects particles larger than 1 µm in diameter. Particles were classified in the range 1 to 16 µm in 15 bins of 1 µm width each assuming the particles to behave as droplets. Further details are given in Appendix 1. Visual observations are documented by color photographs, two video cameras, and a TV camera. The photographs and the cockpit video camera record also the time of observations.

The ATTAS pilots noted data, at times as indicated by the circles in Figure 1a, of flight level FL (in hectofeet (hft)), fuel flow $\dot{m}_F$, exit gas temperature EGT, percentage speed of the low-pressure compressor N1, and true air speed V. The values of $\dot{m}_F$ and N1 were the same for both engines within the accuracy of the instruments readings. The indicated EGT was systematically 10 K lower for the right engine than for the left, possibly due to different calibrations of the EGT sensors. Similar differences were observed in the previous experiment with the same engines [*Busen and Schumann*, 1995]. At that time, no visible differences were found between the contrails formed from the two engines. Hence we assume that the engines were sufficiently equal and do not cause different plume properties. The actual aircraft mass M has been estimated according to takeoff weight and fuel consumption with time. Based on speed, mass, and known drag coefficients of the ATTAS, the aerodynamic drag force is determined to estimate the thrust F of each of the two engines. The climb velocity w is estimated from the altitude readings. Table 3 lists the ATTAS flight parameters. The data represent mean values for both engines during the various phases. The column LH refers to the time period of particle measurements with different fuels. The propulsion efficiency $\eta = (FV + gwM/2)/(\dot{m}_F Q)$ includes the (small) contribution from potential energy gain during climb (g gravity). A thermodynamic engine analysis has been performed to estimate the engine exit conditions, see Appendix 2, with results as listed in Table 4.

The observations took place during one flight on March 22, 1995, between 1020 and 1200 (all times refer to UTC), on a flight from Oberpfaffenhofen near Munich in southern Germany in northern direction to a turn point near Magdeburg in central Germany and retour. The flight occurred below the tropopause, under stably stratified conditions with little turbulence (bulk

Table 2. Falcon Instrumentation

| Parameter	Instrument	Resolution	Accuracy	Response Time	Sampling Rate, Hz
Temperature T	Rosemount platinum resistance thermometers Pt100 and Pt500	0.006 K	0.5 K	0.03 s	100
Static pressure p	Rosemount transducer 1201F2	0.06 hPa	1.2 hPa	0.015 s	100
Horizontal wind u, v	Five-hole pressure noseboom tip and inertial navigation system	0.03 m s^{-1}	1.5 m s^{-1}	0.01 s	100
Vertical wind w	same	0.01 m s^{-1}	0.3 m s^{-1}	0.01 s	100
Relative humidity RH	Vaisala HMP35 capacitive polymer HUMICAP-H	0.01	0.05	10 s	10
Water vapor mixing ratio m	Lyman-α hygrometer, Buck Research L5	1 mg kg^{-1}	4%	6 ms	100
Horizontal position	Honeywell inertial reference system LASERREF YG 1779 and global positioning system (GPS), flight management computer Global GNS-X	20 m	500 m	0.2 s	10
Particle concentration N for sizes d > 7 nm	modified TSI 3760 condensation particle counter CPC	0.2 to 35,000 cm^{-3}	1 nm size	1 s	4
N, d > 18 nm	same	same	2-nm size	1 s	4
N, 0.1 to 1 µm	PMS passive cavity aerosol spectrometer probe PCASP	4 to 10,000 cm^{-3}	50% size	1 s	1
N, 1 to 16 µm	Forward scattering spectrometer probe PMS FSSP-100	0.02 to 1000 cm^{-3}	25% size	1 ms	1
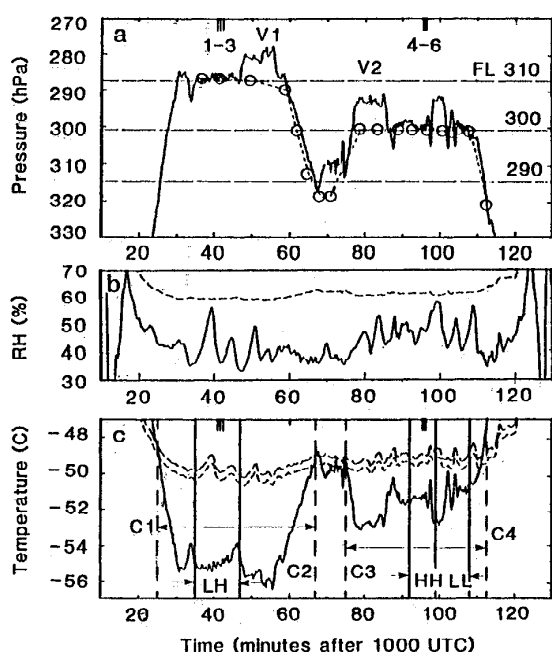
Figure 1. Observations versus time in minutes after 1000 UTC. (a) Pressure versus time of Falcon (solid curve) and ATTAS (dashed with circles), with flight levels (FL in hft) indicated. V1 and V2 denote times of observations of the ATTAS through the Falcon bottom windows. (b) Relative liquid humidity measured on board the Falcon (solid) and ice saturation humidity (dashed). (c) Temperature measured on board the Falcon (solid curve), and threshold temperature computed from the Falcon observations of pressure and humidity using a propulsion efficiency of $\eta = 0.16$ (short dashed) and $\eta = 0.2$ (top curve, long dashed). The vertical solid lines with arrows embrace the time intervals with low or high (L; 170 ppm, H; 5500 ppm) sulfur fuels usage on the left and right engine, LH, HH, LL. For LH, the limits indicate the time period when the Falcon performed measurements within the ATTAS plume. The vertical dashed lines indicate the approximate times of contrail onset or disappearance. Contrails were visible between C1 and C2, and between C3 and C4. The marks at the top of Figures 1a and 1c indicate the times of passes 1 to 3 and 4 to 6.

Richardson number greater than 1). Figure 1 shows the flight data as obtained with the Falcon (5 s mean values) and the pressure read on board the ATTAS versus time. Figure 2 shows the flight path, the locations of various radiosondes, and the displacement of the air with wind during 1 hour. Figure 3 shows the data from the three most characteristic radiosoundings (started at 1100) together with the sounding of the Falcon. Figures 1 and 3 show also the threshold temperature T_{LC} which is computed as described in section 4.1. Contrails were to be expected when the air temperature T is below T_{LC}.

The Falcon measurements, see Figure 1, indicate temperature and humidity variations of ± 1 K and $\pm 10\%$ at constant altitude. Compared to the radiosoundings, the Falcon data show generally about 0.5 K higher temperatures and 10% higher humidity. The temperature near Munich increased by about 1.5 K during the measurement period. The meteorological conditions of this day were determined by strong advection of slightly warmer and more humid air from north, explaining the variability observed. Above 2 km, the sky was generally free of clouds, but on three occasions (1121, 1135, 1142) the video shows the Falcon flying for a short time through thin cirrus clouds or regions with reduced visibility. The measured humidity was above 50% at those times, not much below ice saturation (63%).

As indicated in Figure 1, the ATTAS cruised at altitudes up to FL 310 (9450 m). Four times (C1 to C4), the ATTAS passed through the level above which contrails form. The ATTAS burnt different fuels on different engines separately from takeoff until 1132, and from 1148 to landing. Both engines were supplied with the high (H) sulfur content fuel from 1132 to 1139, and with the low (L) sulfur fuel from 1139 till 1148. At various times the Falcon followed the ATTAS in close formation flight (approaching up to 50 m), made in situ measurements at distances, as determined by the Falcon radar, between 2.8 and 5.6 km behind the ATTAS (plume ages between 17 and 29 s) in the three phases LH, HH, and LL, by repeatedly penetrating the ATTAS contrail from left to right and reverse, and climbed 150 m above the ATTAS to observe the contrail through the bottom windows of the Falcon (V1 and V2), see Figure 1.

3. Results

3.1. Visual Observations

From the visual observations, as documented by videos and photos, we find that the two contrails forming from the two

Table 3. Observed ATTAS Flight Conditions During the Various Phases

Parameter	LH	HH	LL	C1	C2	C3	C4
Time, UTC	1035-1047	1132-1039	1139-1048	1025	1107	1115	1152:30
FL, hft	310	300	300	288	290	290	290
V, m s^{-1}	163	163	163	163	163	163	160
w, m s^{-1}	0	0	0	0.8	-1.4	0.8	-1.5
$\dot{m}_F$, kg s^{-1}	0.164	0.157	0.150	0.170	0.139	0.157	0.126
EGT, °C	452	452	442	460	425	445	409
M, Mg	18.65	17.70	17.55	18.75	18.25	18.05	17.42
F, kN	7.26	7.07	7.03	7.30	7.18	7.12	7.00
η	0.168	0.171	0.178	0.172	0.175	0.182	0.198
p, hPa	287 ± 2	301 ± 2	301 ± 2	317 ± 5	316 ± 2	315 ± 3	316 ± 2
T, °C	-55.0	-51.3	-51.0	-49.0	-49.5	-49.2	-48.3
	± 0.5	± 0.5	± 0.8	± 0.5	± 0.3	± 0.5	± 0.3
RH, %	40 ± 10	45 ± 10	45 ± 10	42 ± 10	36 ± 5	37 ± 10	37 ± 5

Abbreviations are FL, flight level; V, true air speed; w, climb velocity; $\dot{m}_F$, fuel flow; EGT, indicated exit gas temperature; M, mass of aircraft; F, thrust per engine; η, overall propulsion efficiency; p, ambient pressure; T, temperature; RH, relative humidity.

Table 4. Computed Engine and Plume Parameters

Parameter	LH	HH	LL	C1	C2	C3	C4
T_C, K	624	626	615	638	596	622	582
T_B, K	253	244	237	256	220	243	212
v_C, m s⁻¹	482	478	477	472	476	470	466
v_B, m s⁻¹	301	288	284	292	271	284	263
AFR	58	63	67	59	78	65	86
T_{LC}, °C	-50.1	-49.4	-49.3	-49.0	-49.3	-49.2	-49.0
D_{Li}, m	2.18	2.50	2.47	-	-	-	-
D_{LM}, m	2.80	3.11	3.06	3.50	3.07	3.30	3.09
n_{LM}	2800	3730	3780	4560	4260	4360	4650
m_{LM}, g kg⁻¹	0.143	0.053	0.047	0	0	0	0
S_{LM}, %	44	16	14	0	0	0	0
D_{fi}, m	13.8	11.3	10.7	8.7	7.3	7.7	6.4

Abbreviations are T_C, engine core exit temperature; T_B, same for bypass; v_C, engine core exit jet speed; v_B, same for bypass; AFR, air/fuel mass flux ratio in the core engine; T_{LC}, threshold temperature for liquid contrail; D_{Li}, diameter of plume when reaching saturation for water; D_{LM}, diameter of plume for maximum water saturation; n_{LM}, air/fuel mass mixing ratio at maximum liquid water content; m_{LM}, maximum liquid water content; S_{LM}, maximum liquid water supersaturation; D_{fi}, diameter of plume when humidity drops below ice saturation.
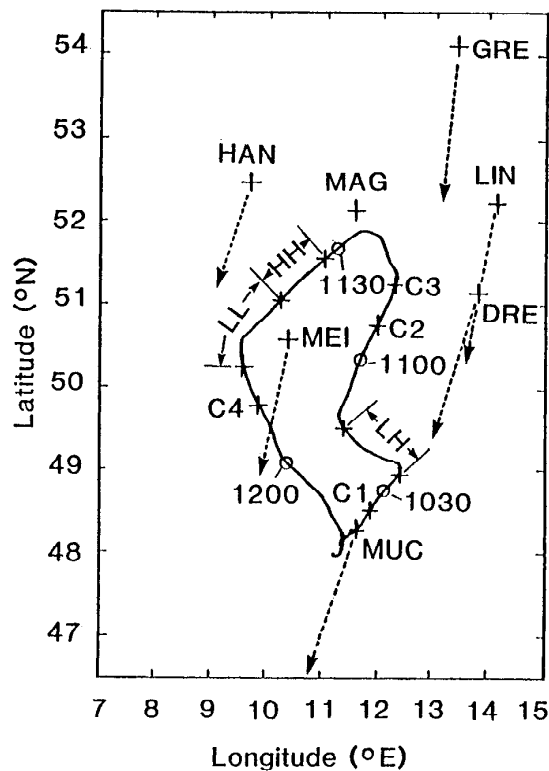
Figure 2. Map of latitude versus longitude with the flight track of the Falcon versus time (every 30 min is indicated by a circle), and the positions of radiosondes Munich (MUC), Meiningen (MEI), Greifswald (GRE), Hannover (HAN), Lindenberg (LIN), Dresden (DRE), and the position of Magdeburg (MAG). The vectors represent the advection due to wind at 300 hPa within 1 hour. C1 to C4 denote positions of contrail onset or disappearance. The in situ measurements took place in the phases LH, HH, and LL, with low (L) and high (H) sulfur on left and right engine, respectively.

engines have different properties when using different fuels. Plate 1 shows a print of a video scene of the ATTAS flying at FL 310, with ambient conditions close to those listed for LH in Table 3. We clearly see the contrails forming from the two engines. The visibility is best over dark surfaces (forest). Obviously, the visible particles form first at the outer edge of the jet plume [*Kärcher*, 1994], leaving a wedge of reduced contrast in the center of the plume. Based on the known wing span and length of the aircraft, we can measure the plume dimensions from this picture. The right contrail becomes visible, still very weakly, first at a distance of about 10 m after the engine exit with an apparent diameter of about 1.3 m. The left contrail forms about 5 m later with a diameter of about 1.7 m. From a similar TV camera scene (1056) for the same altitude, the plume scales were measured as listed in Table 5. Hence the right contrail forms more than 5 m earlier and exhibits about 10 to 20% larger visible diameter up to plume ages of at least 0.5 s. When both engines burnt the same fuel (phases HH and LL) we could not observe differences in plume formation, but the Falcon was usually not in good enough positions to exclude such differences definitely.

Plate 2 documents that the two contrails appear with slightly different colors when viewed with the Sun in the back of the observer. Both contrails are darker than the underlying cloud cover. Obviously, the contrails absorb or scatter part of the radiation reflected from the lower clouds and this reduction in upward radiance is not balanced by the amount of solar radiation scattered upward from the contrails to the observer. The right contrail appears to be slightly brown colored while the left is more grey. This difference was clearly noted by the observers during flight and is documented in several further photos and the videos. When viewed from above, the right contrail is darker than the left one, indicating lower transmission of light reflected from the cloud layer below the contrails. As will be explained below, the change in optical properties may be due to soot immersed in the particles or due to a changed particle size spectrum. Plate 3, taken while flying southward with the Sun ahead slightly to the left, shows both contrails to appear white relative to the clear sky but with higher contrast and earlier onset of the right contrail. The first few meters of the plume were always invisible, without any visible smoke from soot emitted.
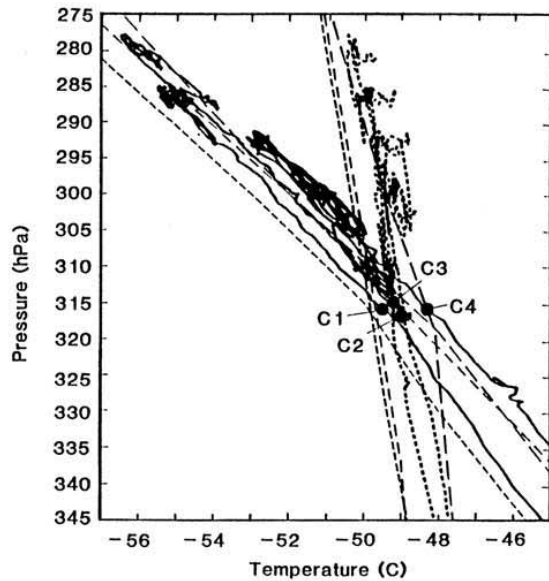
Figure 3. Temperature T and threshold temperature T_{LC} (for $\eta = 0.18$) versus pressure. Thin curves: radiosoundings of Munich (short dashed), Meiningen (medium dashed), and Greifswald (long dashed). Thick curves: Falcon data (solid curves for temperature, dotted curve for threshold). Observed threshold conditions for contrail formation (C1 to C4) indicated by solid circles.

On the same flight leg, the videos show that the contrail contrast changed with distance from the ATTAS. For the first 200 m the right plume gave higher contrast than the left one, but with growing distance the contrast difference reversed. Moreover, the left contrail stayed slightly longer. This indicates a change in the particle size spectrum as a function of sulfur content. It appears that the right engine, with high sulfur fuel, produces more particles. For the same water content this leads to smaller water particles and hence a higher contrast. When the humidity gets reduced in the plume the smaller particles evaporate sooner.

From a series of photos and videos taken during the two descents, C2 and C4, we can identify the times of contrail disappearance to occur between 1105:31 and 1106:45 (C2) and 1152:15 and 1152:48 (C4). These timings are used to identify the ambient air conditions from the Falcon data, accounting for the fact that the Falcon was about 50 m lower than the ATTAS for C2 but 50 m higher for C4. From the photos, it appears as if the right contrail, from high sulfur fuel, persists slightly longer. The right contrail disappears at about 25 to 50 m lower altitude (0.2 to 0.4 K higher temperature) than the left contrail. For the contrail onset during ascents (C1 and C3) the timing is less accurate: C1 between 1024:16 and 1029:48, C3 between 1113:35 and 1118. Table 3 lists the best estimate times together with the experimental conditions for these times. At 1120, the ATTAS contrails at FL 300, observed through the bottom windows of the Falcon, was occurring intermittently, with contrails visible 35 to 45 m after engine exits. Slightly shorter distances (25 to 35 m) were found under onset conditions by *Busen and Schumann* [1995], possibly because of different flight speeds.

Plate 1. Printed video scene with view from the Falcon 150 m above the ATTAS aircraft at 1055 UTC, 49°50"N, 11°30"E, ATTAS at FL 310 (9450 m), burning fuels with different sulfur contents (170 ppm left, 5500 ppm right).

When penetrating the plumes at distances of about 4 km, the contrail pair observed from the Falcon showed a U-shaped structure. Obviously, the jet exhaust moves with the trailing vortex system generated by the aircraft. Since the engines are located close to the plane of symmetry, the jet plumes first move downward with the downward motion in the middle of the vortex system. When reaching the lower edge of the vortex pair, the two plumes circulate symmetrically first sideward and then upward along the outer parts of the vortices. In more humid air, the contrails form an annulus around the vortex axis but the U shape results when the contrails evaporate before getting fully rotated around the vortex. Similar structures have been computed by *Miake-Lye et al.* [1994] for the concentration of exhaust gases in similarly aged contrails, but for a different type of aircraft. Data from flights through this structure were clearly assignable to the different plumes. Unfortunately, slight curves of the ATTAS

Table 5. Diameter of Visible Plumes at Various Distances Behind Engines in Phase LH

	Distance, m				
	10	19	30	60	90
High sulfur D, m	1.6	2.2	2.8	3.3	4.1
Low sulfur D, m	-	2.1	2.2	3.0	3.2

Plate 2. Photo of the ATTAS flying with different fuels as seen from the Falcon cockpit at a distance of about 150 m, at 1100:25 UTC, at FL 307 (9360 m) on a course toward NNE.

Plate 3. Photo of the ATTAS flying with different fuels as seen from the Falcon cockpit at a distance of less than 100 m, at 1128:12 UTC, at FL 300 (9140 m) on a course toward SWS.

flight track or sheared and wavy air motions often caused non-symmetric plume structures.

3.2. In situ Measurements of Plume Properties

The plume data including turbulence and aerosol measurements from six passes through the ATTAS contrail presented here were chosen from visual inspection of the video and notes taken during the flight. The purpose for the selection was to find periods when one visually could resolve the two engine plumes through a more or less well-defined contrail in order to compare with data. The first three passes were taken from phase LH, the second three passes from phase HH. The times of plume penetrations, that is, the times when the Falcon measured maximum downward velocity $-w$, are listed in Table 6 and indicated in Figure 1.

Figure 4 shows, for example, the measurements during pass 1, penetrating the plume from right to left. The particle data were shifted in time by about 1 s to correct for different delay times

such that the data give a symmetric picture. The turbulence outside the plume, in terms of horizontal velocity fluctuations u along 20-s flight segments, is about 0.2 m s^{-1} for passes 1 to 3 and 0.5 m s^{-1} for passes 4 to 6. Obviously, the two engine plumes can be clearly identified from increases in water vapor mass ratio m, temperature T, and particle concentrations N, and from the lateral and vertical velocities v and w in the trailing vortex. Some characteristic values are listed for all passes in Table 6. The plume penetrations lasted for 3 to 5 s. Based on the angle between the headings of the Falcon and the ATTAS (3° to 4°), the effective width of each jet plume (half wake) is 15 ± 4 m in terms of data for humidity and 22 ± 5 m for particle number density. The cross-stream velocity pattern indicates that the plume was penetrated above the plume vortex axis for all passes. It is interesting to note that the particle number density is maximum at the outer edges of the plumes, associated with positive vertical velocity. Pass 1 is the one with the highest relative humidity in the plume, even exceeding ice saturation (RH = 60%); all others are below ice saturation. Otherwise, the mea-

Table 6. Plume Data During Passes 1 to 6

Pass	1	2	3	4	5	6
Time, UTC	1040:57	1041:42	1042:32	1135:25	1135:54	1136:24
Age, s	19	20	22	25	26	27
ΔT, K	0.19	0.22	0.24	0.23	0.22	0.15
Δm, mg kg^{-1}	8.3	7.8	8.3	9.0	9.0	7.6
η_P	0.78	0.96	0.98	0.86	0.84	0.66
D_T, m	23	21	20	18	18	22
D_m, m	20	21	20	19	19	21
u_{max}, m s^{-1}	0.9	1.0	2.3	1.5	0.9	1.0
v_{max}, m s^{-1}	4.0	2.8	4.0	5.6	1.3	1.2
$(-w)_{max}$, m s^{-1}	3.4	3.1	10	7.8	2.0	2.3
RH$_{max}$, %	65	56	48	45	42	52

Abbreviations are ΔT, mean temperature increase above ambient values; Δm, increase in water vapor mass ratio; η_P, $EI_{H_2O}c_p\Delta T/\{(1-\eta)Q\Delta m\}$; D_T, plume diameter based on ΔT; D_m, same for Δm; u_{max}, maximum velocity in ATTAS flight direction; v_{max}, velocity amplitude perpendicular to the plume axis; $(-w)_{max}$, maximum downward velocity; RH$_{max}$, maximum relative humidity.
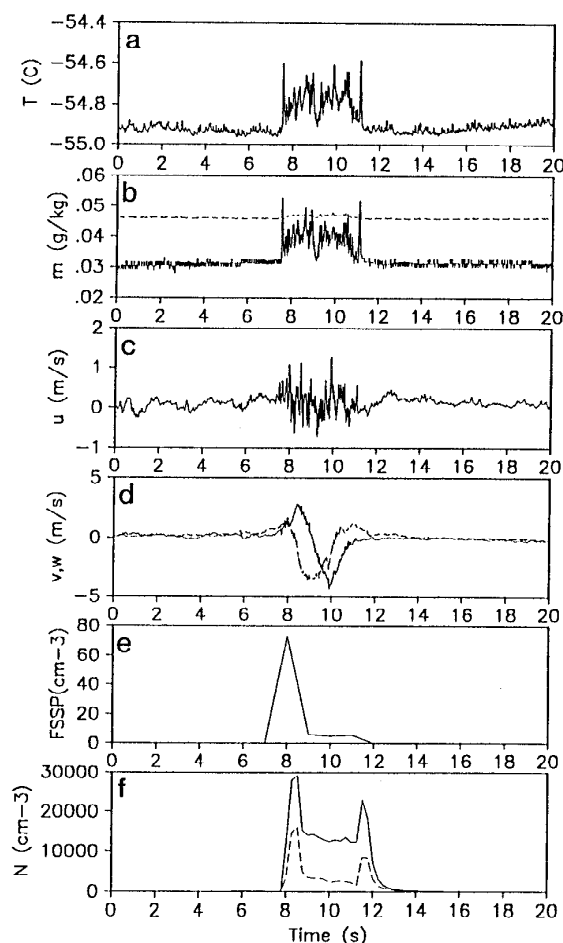
Figure 4. Plume properties during pass 1 versus time in seconds after 1040:47 UTC, penetrating the plume from right to left. (a) Temperature T. (b) Water vapor mass fraction m (solid) and its ice saturation value (dashed). (c) Velocity fluctuation u in the ATTAS flight direction. (d) Cross-plume and vertical velocities, v (solid) and w (dashed). (e) Number density of particles larger than 1 μm diameter measured with the FSSP. (f) Number density of particles N larger than 7 nm (solid) and larger than 18 nm (dashed).

sured profiles are similar for passes 1 to 3, but slightly less coherent in terms of turbulence data for passes 4 to 6.

As a check for consistency of the measured temperature and water vapor changes in the plume, ΔT and Δm, we have computed the ratio $\eta_P = EI_{H_2O}c_p\Delta T/\{(1 - \eta)Q\Delta m\}$ for given emission index EI_{H_2O}, specific heat capacity c_p, and specific heat of combustion Q. This ratio should be one for similar mixing of heat and water vapor. From Table 6 we see that this ratio is a little smaller than 1, which may be due to the limited accuracy of the measurements or due to stronger cooling than water vapor dilution in the plume. Radiative heat losses from the contrails [Knollenberg, 1972] are too small to explain stronger cooling. However, the deviations of η_P from 1 are small enough to justify further evaluations.

From the measured mean temperature and humidity changes and the known amount of emitted water and heat, we compute effective cross sections of the diluted plumes $(\pi/4)D_T^2 = \dot{m}_F Q(1 - \eta)/(\rho_{air}Vc_p\Delta T)$ and $(\pi/4)D_m^2 = \dot{m}_F EI_{H_2O}/(\rho_{air}V\Delta m)$, with air density ρ_{air}. The resultant diameters D_T and D_m are listed in Table 6. We see that the plumes were diluted to effective diameters D of 20 ± 3 m.

3.3. Results from Particle Measurements

Data from the different particle counters are plotted in Figures 5 and 6 for passes 1 to 6, scaled to the same time interval as for pass 1 and such that the exhaust from the right engine is in the right part of the figure and the exhaust from the left engine is in the left part of the figure. From Figure 5 one can see that the exhausts from the different engines are clearly resolved by the two CPCs for all six passes. The PCASP data, see Figure 6, show maximum values inside the plumes and the different plumes can be discriminated only for pass 1. The signal of the contrail in the PCASP is essentially coming from three channels corresponding to particle diameters between about 120 and 160 nm and no significant change could be seen for larger particle sizes. In Figure 5a, for different fuels in the engines, there is an
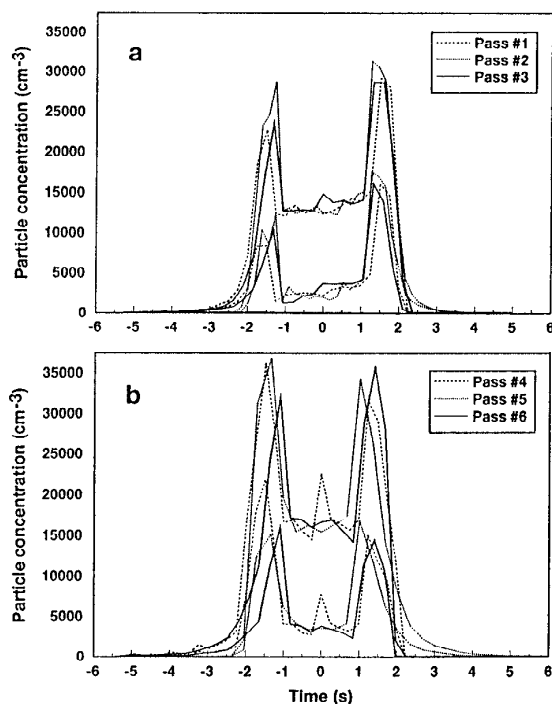

Figure 5. (a) Aerosol number concentration versus time for particles larger than 7 nm (top curves) and larger than 18 nm (bottom curves) in diameter from three passes through the plumes, while using fuel with elevated sulfur content in the right engine (LH). (b) Same as in Figure 5a, but using fuel with elevated sulfur content in both engines (HH). In order to scale the results to the same plume width, the timescale has been multiplied with factors 1, 0.72, 1.06, 0.99, 1.35, 1.12, for passes 1 to 6, respectively, before plotting.
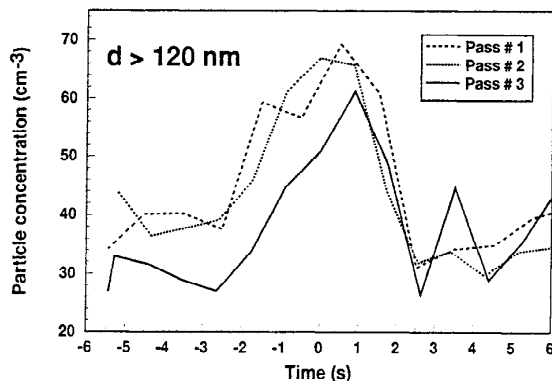
Figure 6. As Figure 5a, for particles larger than 120 nm diameter, for three passes within phase LH.

Figure 7. Additional aerosol volume in the plumes of phase LH. The integral in the figure is about 0.35 $\mu m^3 cm^{-3}$ or 0.35×10^{-12}.

evident difference between the particle concentration from the right and left engine. The difference in concentration is most clear for particles larger than 18 nm with peak values of around 10,000 cm^{-3} and 15,000 cm^{-3} for the respective engine. Between the two peaks there is a trend with decreasing concentration from right to left. Although the trend is not dramatic, it is consistent in the three passes from almost 5000 cm^{-3} down to about 2000 cm^{-3}. For particles larger than 7 nm the concentrations reach about 25,000 to 30,000 cm^{-3}. However, the relative difference between the two peaks is less than for particles larger than 18 nm.

The maximum concentrations observed in the HH passes 4 to 6 (Figure 5b) are consistent with the peak values observed in the concentration for the right engine exhaust in Figures 5a. In general, the concentrations in the HH passes are (about 15%) lower for $d > 18$ nm and higher for $d > 7$ nm with respect to the right engine exhaust in passes 1 to 3 in LH. This could be due to slightly larger distances behind the ATTAS aircraft but also due to the different ambient conditions. In particular, the contrail experienced less water supersaturation in phase HH compared to LH. The background concentration observed by the PCASP was also different for the two phases, about a factor of 2 smaller in phase HH compared to LH.

We show no data for phase LL because the contrail was shorter and the plume structure, possibly because of higher ambient air turbulence, was less clear in this phase. However, the data from this phase are consistent with the other results in showing the same magnitude of particles larger than 7 nm as for HH but less particles larger than 18 nm.

From the measurements in passes 1 to 3 we compare the volume distributions of the particles. The difference between the average size distributions within the plume and outside the plume is shown in Figure 7. The volume of particles greater than 0.12 μm is insignificant outside the plume. Hence most of the aerosol volume in the plume formed from exhaust particles rather than from ambient preexisting particles. The total specific volume is computed as 0.35×10^{-12}. Note that for particles larger than 0.2 μm the uncertainty in concentration is high due to poor counting statistics and that a small change in number concentration can have a large effect in particle volume.

To visualize the data in Figures 5 better and to show how the particle concentration in the exhaust responds to different sulfur containing fuel, we compare the areas under the curves to the
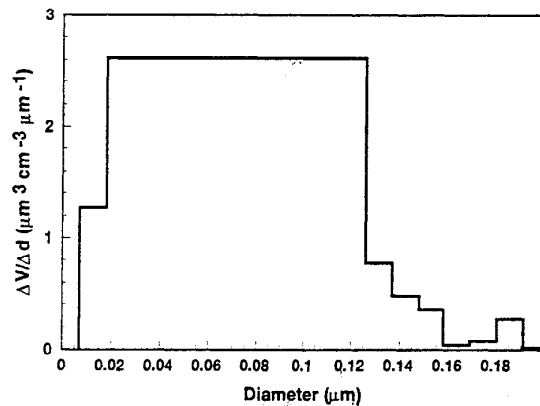
right and to the left of the zero mark in the figures, that is, from the particles generated by the right and the left engine. For particles larger than 7 nm the calculated ratio is about 1.25 and more than 1.5 for particles larger than 18 nm, see Figure 5a. The average ratios for the data in Figure 5b are very close to 1. All the individual ratios are plotted in Figure 8. We are aware that this ratio is a very crude measure and that the exhaust is intermixed, diluted and aged from the time it is emitted till it is sampled. However, all processes can only serve to mask any initial differences in the young plumes.

The FSSP probe identified particles only in a very few contrail penetrations. In most cases the data show particles only in the first size bin (1 to 2 μm). The measured concentrations were typically less than 5 particles per cm^3. Only for pass 1, see Figure 4, when the Falcon was closest to the ATTAS (distance about 3 km), the number density reached 70 cm^{-3} in the first and less than 0.02 cm^{-3} in the second bin (2 to 3 μm). The computed water content stays below 0.15 mg kg^{-1}. In this case, the contrail
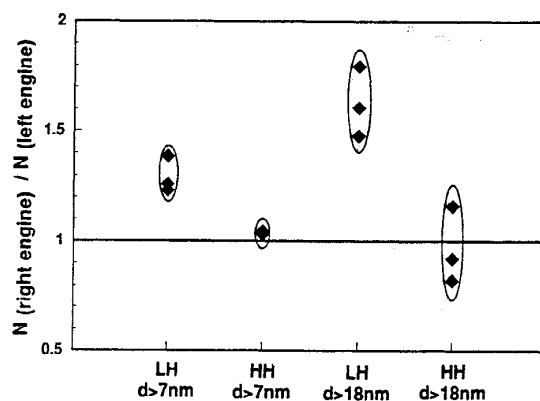

Figure 8. Ratio between the number of particles observed in the exhaust plumes from the right engine compared to that from the left engine, for phases LH and HH and for different detection limits of the particle diameters. The oval lines are to guide the eye.

is clearly visible in the video. Particles were counted mainly in the right plume for this pass. In all other cases, because of larger plume dilution, most of the particles of this size were already evaporated. Ice particles in contrails growing in supersaturated air or in natural cirrus are often larger, typically 15 to 50 μm, with number densities of the order 0.1 to 1 cm⁻³, and ice contents up to 10 mg kg⁻¹ [*Gayet et al.*, 1996].

4. Discussion

The observations provided data on plume and contrail scales. Moreover, the observations show differences between the left (low sulfur) and right (high sulfur) contrails. In this section we first examine how far the observed contrail properties can be explained with simple thermodynamical concepts and estimate the degree of supersaturation and the amount of liquid water in the contrails. Then we interpret the observations to explain the observed differences between the left and right plumes using order of magnitude estimates. Finally, some implications are discussed. The notation section lists frequently used symbols.

4.1. Plume Dimensions and Comparison to the Schmidt/Appleman Theory

The measurements show plume diameters D of about 2 m at the onset of contrails and diameters of about 20 m at a plume age of 20 s. Later studies might compute the mixing process with proper fluid dynamics codes [*Miake-Lye et al.*, 1993, 1994; *Kärcher*, 1994]. Here we use simple estimates for orientation and as a test for consistency between the various data obtained.

For conservation of momentum, the plume air receives the thrust F of the engines so that the bulk plume velocity V_j relative to ambient air satisfies $F = \rho_{air}(\pi/4)D^2VV_j$ for all times. For a plume diameter of 2 m, the jet velocity is $V_j = 31$ m s⁻¹, causing strong shear mixing. For the diameter of 20 m during the in situ measurements it decays to 0.3 m s⁻¹. This value is of the same order as the measured axial velocity fluctuation u, see Figure 4 and Table 6. The aircraft, with wing span $B = 21.5$ m, induces a vortex system with vortex axis separation of $\pi B/4 \cong 17$ m [*Miake-Lye et al.*, 1993; *Schumann*, 1994], which is larger than the separation of 6.1 m between the engines, as expected from the U-shaped contrail structure. The vortex roll-up time is short, about $1.5\rho_{air}VB^3/(gM) \cong 6$ s. The vortex system moves downward as a whole with a velocity $w = 8gM/(\pi^3\rho_{air}B^2V) \cong 1.4$ m s⁻¹. The velocity in the plane of symmetry reaches 4 times this value, which agrees approximately with the measured values of $-w_{max}$ listed in Table 6. Within the first 30 s, the vortex moves downward about 40 m. Hence vortex and jet motions explain the observed mixing of each plume to the effective diameters of about 20 m within the first 30 s.

The Schmidt/Appleman theory [*Schmidt*, 1941; *Appleman*, 1953], as described in detail by *Schumann* [1996], is applied to check how far the measured contrail parameters can be understood thermodynamically. When the hot and moist exhaust gases mix with the ambient air, the mixing follows along a straight line in the diagram as shown in Figure 9, depicting the water partial pressure as a function of temperature in the plume. The environmental state is at point E and the exhaust conditions at the jet exit is far outside the diagram. The mixing line has a slope $G = EI_{H_2O}c_pPR_{H_2O}/[R_{air}Q(1-\eta)]$, depending on ambient pressure p and the gas constants R for water vapor and air. As illustrated in Figure 9, a contrail may form by liquid condensation when the
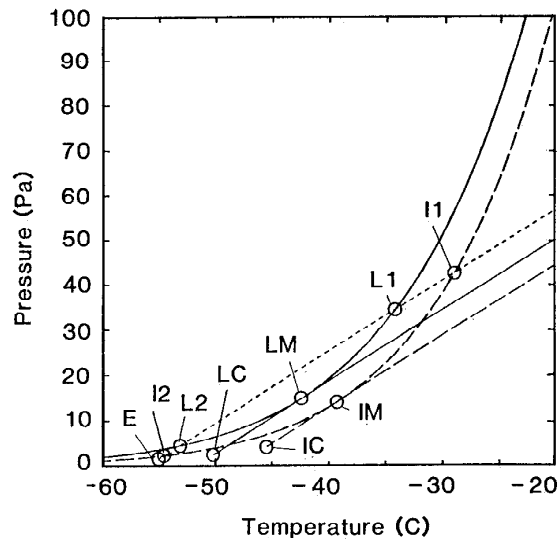

Figure 9. Water vapor partial pressure versus temperature with saturation for water (solid curve) and ice (dashed curve) and lines of isobaric mixing for conditions as in phase LH for contrail onset at liquid water saturation (solid) and ice saturation (long dashed) and ambient temperature (short dashed). For environmental conditions at point E, the mixing passes through points I1 and L1 of initial ice and liquid saturation, and then L2 and I2 of final liquid and ice saturation. At LM and IM the plume reaches liquid or ice saturation under threshold conditions with ambient conditions at LC or IC.

environmental temperature is below the threshold temperature T_{LC}. In this case mixing causes liquid saturation at temperature T_{LM}, where the saturation pressure $e_s(T)$ has the same slope as the mixing line, $de_s(T_{LM})/dT = G$, and where the mixing line connects the states at point LM and LC: $e_s(T_{LM}) = RH$ $e_s(T_{LC}) + G(T_{LM} - T_{LC})$. Similarly, the points IM and IC follow for ice saturation. For $T_E < T_{LC}$, the plume passes through saturation first with respect to ice (I1), then for liquid water (L1), reaches maximum saturation first for ice (IM) and then for liquid water (LM), and then dilutes again to saturation for liquid water (L2) and ice (I2). The temperature excess ΔT in the plume above ambient temperature T_E is related to the dilution factor, that is, the mass of air mixed with the exhaust of burnt fuel mass, $n = Q(1-\eta)/(c_p\Delta T)$. For given fuel flow the corresponding plume diameter satisfies $(\pi/4)D^2 = nm_F/(V\rho_{air})$. Some of the corresponding state parameters are listed for all flight phases in Table 4. For phase LH with $T_E = -55°C$, the plume temperatures are -28.9°, -34.1°, -42.3°, -53.1°, -54.5°C, at points I1, L1, LM, L2, and I2, respectively.

Figure 3 shows the ambient temperature and the threshold temperature T_{LC} as computed for the given heat and moisture emissions of the ATTAS as a function of pressure and humidity. For the temperature and humidity data derived from the radiosoundings, contrails were to be expected at altitudes above pressure 317 hPa (FL 288), roughly consistent with the observations. For the Falcon data, the contrail onsets were observed at temperatures which differed from the threshold temperatures by less than 0.7 K; see Figure 1c. *Busen and Schumann* [1995]

found similar agreement. The observed plume diameters at contrail onset for phase LH (Table 5) of about 2 m is close to the computed value $D_{LI} = 2.15$ m. The computed diameter of $D_{I2} = 13.6$ m of the contrail when diluted below ice saturation appears also to be realistic when compared to the visual observations. The ice content observed with the FSSP is about a factor of 1000 less than the maximum possible water content. Obviously, the measurements were taken behind the point 12, with few remaining ice particles. No contrails were observed when the air temperature was in between T_{LC} and $T_{IC} \cong -45°C$ where the plume moisture exceeds ice saturation. These results support the common view that the visible particles in contrails form via the liquid phase, freeze at least partly, and then evaporate from the ice phase.

4.2. Differences Caused by Different Levels of Sulfur Emissions

The right engine burnt a fuel with a very high sulfur content S of 5500 ppm, higher than the specification limit of 3000 ppm, about 10 times larger than the average value 420 ppm [Schumann, 1994], and 32 times larger than for the left engine (170 ppm). The larger sulfur emissions cause contrail formation at slightly warmer (< 0.4 K) ambient temperature, earlier contrail visibility after engine exit, changes in the optical properties, a slight increase in the number of particles larger than 7 nm, and a shift in particle size with 50% more particles larger than 18 nm.

The increase in sulfuric acid mixing ratio in the plume can be computed from a mass budget relating the sulfur emissions with the amount of sulfuric acid in the plume of diameter D,

$$[H_2SO_4] = \frac{S \, s \, \dot{m}_F M_{air}}{M_S \rho_{air}(\pi/4)D^2 V}, \tag{1}$$

for given sulfur mass content S in the fuel, number fraction s of sulfur dioxide converted into sulfuric acid, and molar masses of air $M_{air} = 29$ and sulfur $M_S = 32$. For $s = 0.4\%$ [Reiner and Arnold, 1993] (possibly a lower bound of the conversion) and $D = 20$ m, one computes an increase by 140 parts per trillion by volume (pptv) for 5500 ppm sulfur content in the fuel, and by 4 pptv for 170 ppm. These values are much larger than ambient values of sulfuric acid in the upper troposphere of about 0.01 to 0.05 pptv [Möhler and Arnold, 1992]. Even for 1 ppm fuel sulfur content, the additional sulfuric acid concentration is comparable to background values. In any case, the resultant concentration exceeds by far the saturation mixing ratio which is of order 0.001 pptv for -50°C [Hamill et al., 1982]. Hence present levels of sulfur contents in aviation fuels are high enough to make sulfuric acid nucleation very likely.

Nucleation rates increase strongly with supersaturation. Kärcher et al. [1995] computed an increase in nucleation rates by a factor of 200 for an increase in fuel sulfur content from 360 to 3000 ppm and more than a factor of 10^6 increase in particle number density larger than 80 nm diameter, for $T_E = T_{LC}$. Hence we should expect a much larger number density of particles nucleated from the high sulfur fuel than for the low sulfur case and also a larger amount of aerosol volume. However, the observed number densities of particles larger than 7 nm differed by only 25% and the particles larger than 18 nm responsible for most of the aerosol volume changed by less than a factor 2. One

could argue that much of the nucleated aerosol has diameters smaller than 7 nm; however, such small droplets would coagulate quickly and should become larger than 7 nm well before the plume reaches a plume age of 20 s (see Appendix 3). Moreover, as noted before, such small aerosol does not explain why particles grow quickly to form a visible contrail within about 0.3 s after leaving the engine exit [Kärcher et al., 1995]. We conclude therefore that the measured aerosol and the CCN are formed not only by homogeneously nucleated sulfuric acid droplets.

Alternatively, it appears reasonable that the measured aerosol and the CCN responsible for quick visibility of the contrails is formed from soot which gets increasingly activated with growing level of sulfur emissions. The activation may be due to heterogeneous nucleation of sulfuric acid with water at the soot surface or by coagulation between soot and homogeneously formed sulfuric acid droplets or by processes leading to deposition of sulfuric compounds on soot in the process of soot formation in the engines or the hot exhaust. In order to support this possibility, various order of magnitude estimate are given below and compared to the observed facts.

The number of soot particles can be estimated for given emission index EI_{soot} and mean diameter d_{soot} of soot. As described in Appendix 2, the emission index is about $EI_{soot} \cong 0.5$ g kg^{-1}, possibly with an uncertainty of factor 2. The soot diameter is estimated as $d_{soot} \cong 60$ nm, with about the same uncertainty. It is unlikely that the soot particles are much smaller on average, since very small particles would coagulate quickly (see Appendix 3). The soot density is $\rho_{soot} \cong 2$ g cm^{-3} for graphitic carbon, with lower effective values for sponge-like soot. Hence for an initial plume diameter of $D = 2$ m, one computes a particle number density N_{soot} of

$$N_{soot} = \frac{EI_{soot}\dot{m}_F}{\rho_{soot}(\pi/6)d_{soot}^3(\pi/4)D^2 V} \cong 700,000 \text{ cm}^{-3}, \tag{2}$$

with a large uncertainty factor of order 10, mainly because of unknown effective soot diameter. The emission index cannot be much larger than given, because otherwise we should have seen a smoke-forming soot plume. For the given values, the optical thickness of the soot plume is $\tau = D(\pi/4)d_{soot}^2 Q_{ext}N_{soot} \cong 0.002$. Here the extinction efficiency $Q_{ext} \cong 0.35$ to 0.48, depending on the refraction index of soot [Chylek et al., 1984], grows to first order linearly with d_{soot} according to Mie calculations [Van de Hulst, 1957]. The visibility changes little with d_{soot} but depends on $\tau \sim EI_{soot}/D$. In order to become visible, $\tau > 0.02$ is required [Champagne, 1971]. Since smoke was invisible even at the engine exits ($D = 0.4$ m), the emission index EI_{soot} must have been smaller than 1 g kg^{-1}.

The estimated soot particle density is supported by the data of Pitchford et al. [1991] who measured a particle concentration of 300,000 cm^{-3} in the wake of a Sabreliner, 200 m behind the engines with plumes of 5 m diameter. The estimated particle emission of the ATTAS corresponds to an emission index $EI_{part} = EI_{soot}/(\rho_{soot}\pi d_{soot}^3/6) \cong 2 \times 10^{15}$ kg^{-1} of soot particles per fuel mass, again with a large uncertainty factor. About the same value can be deduced from Fahey et al. [1995] who measured simultaneously the particle number density and the CO_2 mixing ratio in the wake of the ER-2 stratospheric research aircraft about 10 min after emission. If the particle number stayed constant up to that plume age, their data reveal values of EI_{part} between 0.4×10^{15} and 4×10^{15} kg^{-1}.

Next we check whether the given soot number density may

be responsible for the early visibility of the contrail by acting as CCN. For flight phase LH, the plume reaches a maximum liquid supersaturation at point LM of 44%. One may expect that this supersaturation causes activation of a large fraction a of the soot particles in the presence of sulfuric acid. In order to become visible many large particles must be formed. Distributing the maximum amount of liquid water, which the Schmidt/Appleman theory predicts to be $m_{LM} \cong 0.14$ g kg^{-1}, equally on a fraction a of the soot particles in the young plume gives droplets with a diameter d_{drop},

$$\frac{\pi}{6} d_{drop}^3 \cong \frac{m_{LM}\rho_{air}}{aN_{soot}\rho_{H_2O}} .$$ (3)

This results in $d_{drop} \cong 0.56$ μm for $a = 1$, and larger values for $a < 1$. At 550 nm wavelength with optical data from Palmer and Williams [1975], particles with $d_{drop} = 0.56$ μm cause an optical thickness of 0.62, 0.7, and 0.82, for pure ice particles, pure water droplets, and droplets with 25% mass fraction H_2SO_4, respectively (even if all H_2SO_4 enters the liquid phase, its mass fraction remains below 0.032% for $s = 0.4\%$). Hence for $a = 1$ the particles form a clearly visible plume for all these types of particles. The optical thickness varies with $(a \, EI_{soot})^{1/3}/d_{soot}$. Hence visible particles are to be expected for a wide range of parameter values. A visible contrail should form even for low values of a of order 0.01, as observed [Pitchford et al., 1991; Hallett et al. 1990]. The earlier visibility of the right plume suggests a larger value of a for the higher sulfur fuel content. Assuming an initial contrail diameter of only 1 m and the previously estimated droplet number density for $a = 1$, the required optical thickness of 0.02 is reached when the particles have grown to diameters of 0.14, 0.13, and 0.12 μm, for the particle types listed above, respectively. The diameters are again similar in magnitude and little dependent on the type of particle.

Obviously, particles with diameters between 140 and 560 nm diameter must have got formed in the plumes within the very short time (0.05 to 0.3 s) after engine exit. From equation (13-2) of Pruppacher and Klett [1980, pp. 420], assuming unit accommodation coefficients as suggested by Wagner [1982], and constant supersaturation of 40%, one computes that pure water droplets grow within 0.012 s from 60 nm to 140 nm diameter, and within 0.28 s to 560 nm. The growth rate depends strongly on the accommodation coefficient. Hence the quick growth of water droplets can be understood only when the accommodation coefficient is close to 1. The particle growth rate may be enhanced when the particles contain considerable amounts of sulfuric acid. However, the quickly growing water droplets take up only little sulfuric acid because its partial pressure is at least 100 times smaller than the water vapor supersaturation pressure. In principle, solution droplets may form already before reaching water saturation and grow quickly after freezing [Heymsfield and Sabin, 1989]. However, the period between I1 and L1, with supersaturation for ice but subsaturation for water, is short and appears to be too warm ($T_{L1} = -34.1$°C) for homogeneous ice nucleation from solution droplets [DeMott, 1990]. Since the observations show that sulfur emissions reduce the time required to form visible contrail particles, we conclude that this is caused by activation of many of the large soot particles by the sulfur emissions. Under threshold conditions ($T_E = T_{LC}$), the maximum water supersaturation will be small and reached late in the plume. In this case, condensation growth is too slow, and early freezing of solution droplets or direct ice nucleation is required to generate a visible contrail as early as observed [Kärcher et al., 1995].

The role of soot getting activated to form CCNs as a function of sulfur emissions is further corroborated by the observed difference in color of the two contrails for phase LH, Plate 2. We first considered the possibility that the different optical properties resulted from spectrally different light absorption by soot immersed in liquid droplets [Chylek et al., 1984] or by soot at the surface of droplets [Chylek and Hallett, 1992]. However, a separate study (K. Gierens and U. Schumann, Colors of contrails from fuels with different sulfur contents, submitted to Journal of Geophysical Research, 1995) showed that the color difference results from changes in the droplet or ice particle spectrum due to different degrees of soot activation. The extinction of light passing through the contrail is stronger in the blue range than in the red range in the solar spectrum when the contrail contains many small droplets instead of few large droplets at the same water content, causing the brownish color. For the visual appearance of the optically thin contrails ($\tau < 1.2$), the soot volume fraction in the droplets is negligible.

When the particle number stays constant in the plume during mixing from 2 m to 20 m diameter, the particle number density gets reduced by a factor of 100. Hence we expect a number density of 7000 cm^{-3} of particles with mean diameter larger 60 nm in the aged plume where the measurements took place. The estimated number density is only a little smaller than the measured value of about 10,000 cm^{-3} in the size range above 18 nm. However, the quantitative uncertainties in these estimates are large, and we cannot exclude that a fraction of the measured particles was generated from self-coagulation of homogeneously nucleated sulfuric acid droplets or from very small soot particles which have grown by H_2SO_4/H_2O condensation to this size range.

In order to check whether enough sulfuric acid was available to coat the soot and to increase the particle size as observed, we assume again $s = 0.4\%$ conversion of sulfur into sulfuric acid, and 87% mass fraction of sulfuric acid in particles having passed through the inlet system of the particle counters. (This mass fraction has been computed using the thermodynamical model of Carslaw et al. [1995] with the help of K. S. Carslaw, for $p = 226$ hPa, $T = 300$ K, $[H_2O] = 80$ parts per million by volume, $[H_2SO_4] = 140$ pptv, which approximates the conditions inside the particle measurement systems. For ambient conditions, $T = T_E = 218.7$ K, $p = 287$ hPa, and the same concentrations, the mass fraction is 34%.) Distributing all the sulfuric acid equally on (spherical) soot particles of diameter $d_{soot} = 60$ nm, results in a (thin) acid layer of thickness δ, with

$$\delta = \frac{S \, s \, M_{H_2SO_4} m_F}{0.87 M_S N \rho_{acid}(\pi/4)D^2 V \pi d_{soot}^2} ,$$ (4)

with molar masses $M_{H_2SO_4} = 98$ and $M_S = 32$, fuel sulfur content S, a particle number density $N \cong 10,000$ cm^{-3} as observed, an estimated droplet density $\rho_{acid} \cong 1.8$ g cm^{-3}, and a plume diameter of $D \cong 20$ m as observed. The resultant acid layer is rather thin, $\delta = 1.2$ nm for $S = 5500$ ppm, and would be even thinner if one accounts for the large specific surface of soot particles. For 170 ppm sulfur content in the fuel, one computes $\delta = 0.04$ nm, about a factor of 10 less than the diameter of H_2SO_4 molecules. Hence a sulfur content of 170 ppm is not enough to form one monolayer of sulfuric acid molecules on the soot particles, and only part of the soot particles may get activated for such low sulfur contents. The computations suggest definite changes in a when increasing S from 170 to 5500 ppm, but the fraction a depends strongly on the specific surface of the soot.

For spherical soot particles with $d_{soot} = 10$ nm the coating with sulfuric acid would increase the particle diameter to 30 nm for 5500 ppm and to 12.2 nm for 170 ppm, consistent with the measured 50% increase in particle numbers larger than 18 nm for the high-sulfur case. The measured 25% increase in the number of particles larger than 7 nm may be due to growth of initially very small soot particles or from some homogeneously nucleated sulfuric acid droplets. The number density of particles larger than 18 nm measured in phase LH is larger than that for phases LL and HH. These phases differ in the amount of water available for condensation, see Table 4, with smaller supersaturation in phases LL and HH compared to LH. This suggests that the fraction of aerosol which grows to the measurable size range increases with the supersaturation in the contrail. It would be interesting to observe the particle spectrum in a plume at slightly higher temperatures without forming a contrail.

If one computes the specific volume of soot and sulfuric acid for the given parameter values in the plume with $D = 20$ m, one obtains a specific volume of 0.14×10^{-12} from the sulfuric acid/water and 0.8×10^{-12} from the soot emitted, including all particle sizes. Hence the measured aerosol volume of 0.36×10^{-12}, of particles larger than 120 nm, see Figure 7, can hardly be explained with sulfuric acid alone.

Besides formation of sulfuric acid coating by binary condensation one may also speculate on the possibility that the soot particles take up sulfur components already in the combustion chamber when the soot forms or by adsorbing sulfur dioxide in the hot exhaust soon thereafter. If sulfur compounds are retained in graphitic soot, the formation of mixed soot particles would be one possibility to explain observed sulfur impact on soot and CCN formation [*Haynes and Wagner*, 1981; *Lammel and Novakov*, 1995].

4.3. Implications

Obviously, the sulfur in the gases serves as important precursor for generation of particles larger than 7 nm in the wake of an aircraft. We also observed an increase in the first channels of the PCASP around 0.15 μm diameter. This size range can readily take part in formation of ice cirrus clouds [*Heymsfield and Sabin*, 1989]. If containing soot, this will change the effective absorption efficiency of soot and the optical properties of clouds. Both changes may have a climatic effect. If contrails form in ice-saturated air, they may spread over a large area. Such contrails may persist the longer the smaller the particles are because of reduced sedimentation. Hence contrails may cover a larger region when the number of CCNs emitted gets enhanced by sulfur and soot emissions.

Near the tropopause, the atmosphere is supersaturated with respect to H_2SO_4-H_2O during daytime [*Mirabel and Katz*, 1974; *Arnold et al.*, 1981; *Hamill et al.*, 1982]. Hence the sulfuric acid/water droplets may grow even at low ambient humidity and form an invisible aerosol trail [*Arnold et al.*, 1994; *Frenzel and Arnold*, 1994]. The residence time of such aerosols in the lower stratosphere is of the order of several weeks to months. These time-scales are large enough to cause considerable accumulation of aircraft-induced aerosols [*Hofmann*, 1991; *Pitchford et al.*, 1991]. In the upper troposphere, the aerosol will stay for several days. *Sausen and Köhler* [1994] have computed the dispersion of passive tracers simulating emissions from air traffic with decay times of 4, 10, and 20 days. In view of the high concentration of air traffic in the latitude band from 40° to 60°N, any increase in particle concentrations is most pronounced in this region, with very little impact on the southern hemisphere. For the North Atlantic flight traffic corridor, under assumptions as given by *Schumann* [1994] (500 aircraft daily, consuming 60 Mg of fuel each within a corridor volume of 5000 km × 1000 km × 2 km) and for an emission index of 2×10^{15} particles per kilogram of fuel, that is, for a number of particles given by the number of soot particles emitted, one computes a mean increase in particle concentration of 6 cm^{-3}, if the residence time is 1 day in the corridor, compared to typical background values of 100 cm^{-3} [*Turco et al.*, 1982]. Emissions in the lower stratosphere will have longer residence times, get transported mainly poleward, and may cause enhanced cloudiness in particular near the tropopause. Chemical implications are also conceivable [*WMO*, 1995].

The present levels of sulfur contents in aviation fuels are high enough to cause sulfuric acid concentrations in the exhaust far above ambient values. Even if the fuel would be totally free of sulfur, the engine would still present a source of condensable sulfur compounds by burning ambient air (F. Arnold, personal communication, 1995). Sulfur-containing molecules in the upper troposphere include sulfur dioxide, SO_2 (80 to 500 pptv) [*Möhler and Arnold*, 1992], carbonyl sulfide (400 to 600 pptv) [*Turco et al.*, 1982], and sulfuric acid aerosols (highly variable) [*Turco et al.*, 1982]. The equivalent mixing ratio of the sum of these molecules may amount to about 2 parts per billion by volume. For a typical air/fuel ratio of about 60, a fuel sulfur content of 0.13 ppm would still double this mixing ratio in the undiluted exhaust. Even the case with 2 ppm fuel sulfur content considered by *Busen and Schumann* [1995] is still high enough in this sense and may contribute to sulfuric acid aerosol generation. However, the concentration of sulfuric acid quickly gets reduced with plume dilution. Moreover, the results from (4) suggest that average fuel sulfur contents may be too small to provide enough acid to coat a large fraction of the soot surface.

5. Conclusions

As far as we know, these are the first experiments which demonstrate a visible and measurable influence of fuel sulfur on contrail formation. We found that increased sulfur emissions cause (1) a slightly earlier onset of contrail formation (about 5 to 8 m closer to the engines, about 10 to 20 m behind the aircraft), when the ambient temperature is 5 K below the threshold value for contrail formation; (2) an increase in optical thickness of contrails shortly after onset; (3) about 10 to 20% larger diameter of the visible plumes in the first 200 m; (4) stronger extinction of solar radiation, in particular in the blue range of the solar spectrum, causing a brownish appearance; (5) only a slight increase (25%) in the number density of particles larger than 7 nm, with a shift to larger particle size causing 50% more particles larger than 18 nm, and small changes in particles between 120 nm and 1 μm; (6) a slight reduction in optical thickness of contrails after the first kilometer and earlier contrail evaporation, possibly due to more subvisible particles and less visible ice particles; (7) a slightly longer visibility of contrails during descent, corresponding to less than 0.4 K higher threshold temperature, with contrails forming about 30 to 40 m after engine exit.

The observations provide a rather complete set of data, from the engine exit conditions to a plume age of about 30 s, including measures of the visible plume diameters for the first 100 m, and turbulence data for the aged plume. The plume diameters are

only a little smaller than expected for a homogeneously mixed plume in thermodynamic equilibrium. The contrails first form in the jet mixing layer, as expected [Kärcher, 1994]. After 20 to 30 s, the plumes are mixed to effective diameters of 20 m, the water vapor concentration is diluted slightly below ice saturation, with few remaining visible particles (probably ice), but many subvisible particles (unknown phase). Estimates are given on the amount of soot emission, soot particle size, and resultant particle diameters which are consistent with the optical properties, measured data, previous particle observations [Pitchford et al., 1991; Fahey et al., 1995], and estimates on the amount of sulfuric acid formed for given sulfur emissions.

We cannot definitely decide on how the particles were formed. However, it appears that the measured particles neither originate from ambient aerosol entrained into the plume nor solely from homogeneous nucleation. The weak variation of the particle number with fuel sulfur content, the increase in mean particle diameter consistent with computed acid-coated soot-particle diameters, the change in color, and the estimated timescales for coagulation suggest that a major part of the sulfuric acid condenses with water directly on the soot particles or that most of the homogeneously nucleated droplets coagulate in the young plume with the soot particles. The higher the sulfur content the more of the soot may get activated and immersed in acid droplets or ice particles.

The effects of different fuel sulfur contents were not visible for 250 ppm compared to 2 ppm in the observations of Busen and Schumann [1995]. As they noted, differences might have been present in that case causing measurable differences in particle size spectra but were not measured in their explorative test. A fuel sulfur content between 2 and 250 ppm is large enough to cause considerable increase in condensable sulfur compounds in the undiluted exhaust but may not be large enough to activate a major fraction of the soot particles.

Future experiments should try to measure the content of soot and sulfuric gases in the plume simultaneously with the particle and thermodynamical plume properties in order to identify the amount of sulfuric acid deposited on the soot. Such experiments should be performed with very low (less than 1 ppm) and very high (above 3000 ppm) sulfur content fuels, in plumes above and below the threshold temperature for contrail formation. Also, it would be important for analysis to know more precisely the composition, size spectrum, and specific surface of the soot at the jet exits. Tests with different fuels or engines causing different amounts of soot would provide direct evidence for the importance of soot.

The sulfur content in the jet fuel has only a minor effect on the temperature below which contrails form. However, sulfur emissions cause an invisible aerosol trail. The additional and larger aerosol increases the background level of condensation nuclei and possibly ice nuclei and may cause changes in cirrus cloud formation, in particular in the flight corridors at northern latitudes, near the tropopause, and in regions which otherwise stay supersaturated with respect to ice. However, the magnitude of these effects remains to be investigated.

Appendix 1: Details on the Particle Instruments

The CPCs and the PCASP measured particles in air sampled from outside the Falcon at a total flow rate of about 10 L min⁻¹ through a 1/4" stainless steel tube with a tapered inlet yielding an opening cross section of 3.8 mm². The inlet is located on the roof of the Falcon at a distance of 40 cm from the fuselage to

ensure free-stream sampling, and the opening is facing the opposite direction of flight. This design of the aerosol inlet results in a zero sampling efficiency for particles greater than about 1 µm diameter. From the aerosol inlet the sample air is transported to a flow-splitter inside the aircraft, from which the air is distributed to the different sensors. The time spent by the air in the sampling line before it reaches an instrument is less than 1 s, and the data are corrected for this phase lag. Compared to the ambient air, the sample air will have about 80 K higher temperature when it reaches the sensors with pressure below the outside pressure because of negative pressure head at the backward facing inlet. This results in evaporation of most of the water from the particles [Hofmann and Rosen, 1978].

The CPCs are equipped with new butanol reservoirs and pressure compensating filters in order to reduce sampling problems occurring from working at low pressures and encountering sudden pressure changes [Noone and Hansson, 1990; Zhang and Liu, 1991]. Furthermore, the condensers of the instruments have an extended cooling system which allow operation at different lower detection limits for the two CPCs with similar size resolution as the TSI 3010 type CPC [Mertes et al., 1995]. The 50% detection limits are 7 and 18 nm (10% limits: about 5 and 12 nm, 90% limits: 9 and 28 nm), respectively. The sample flow rate of the CPC instrument is 1.5 L min⁻¹. The logging frequency of 4 Hz corresponds to a spatial resolution of about 40 m along the flight path. The two instruments agree in measured particle concentration within 2 to 3% when operated with the same amount of cooling, that is, the same lower detection limit. The 16 bit counters in the data acquisition system cover an equivalent particle concentration of 10,000 cm⁻³ before being reset. When the concentration exceeds this value, the data have to be corrected by hand. In this procedure, we make sure that the number density of particles larger than 18 nm stays below the value above 7 nm. Due to the design of the optical detection system in the CPCs there is a possibility for coincidence problems when the concentration becomes too high. Therefore the data are multiplied with a correction factor given by the instrument manufacturer. For a measured particle concentration of 10,000 cm⁻³ this correction factor is 1.06, for a concentration of 20,000 cm⁻³ this correction factor is 1.25. At an ambient concentration of about 100,000 cm⁻³ the particle counters are saturated and cannot distinguish between different particles.

The PCASP of Particle Measurement Systems (PMS) is especially designed for low-pressure operation conditions. It covers the size range between 0.1 and 3.5 µm which is divided into 32 size classes. The instrument was calibrated for ammonium sulfate particles up to 1 µm. Due to the design of the aerosol inlet and an erroneous first size bin, the integral number concentration as measured by the PCASP represents particles between 120 nm and about 1 µm diameter. The probes are equipped with mass flow controllers. The volume flow rate depends only weakly on ambient pressure. Although the data were logged at 1 Hz, the low flow rate of the PCASP (0.06 L min⁻¹) results in a significant statistical uncertainty for low ambient number concentrations.

Appendix 2: Engine Analysis and Soot Emission Index

A thermodynamic engine analysis has been performed to estimate the engine exit velocities v_C and v_B, and temperatures T_C and T_B at the core exit (C) and bypass exit (B), respectively, relative to given environmental conditions (E). The parameters

are determined such that the engine provides the given thrust (the exit pressures equal the ambient pressure for this engine) $F = \dot{m}_L(v_C - v_E) + \dot{m}_F v_C + \dot{m}_B(v_B - v_E)$ as a function of core and bypass mass flows $\dot{m}_C = \dot{m}_L + \dot{m}_F = \rho_C A_C v_C^2$, $\dot{m}_B = \rho_B A_B v_B^2$, with $\rho = p/(RT)$, gas constant R, and satisfies the energy budget in terms of total enthalpies $h_t = h + v^2/2$ $(dh = c_p dT$, $v =$ velocity relative to aircraft), $\dot{m}_F(Q - h_{tE}) = \dot{m}_C(h_{tC} - h_{tE}) + \dot{m}_B(h_{tB} - h_{tE})$, for given values of the fuel flow rate $\dot{m}_F$, specific combustion heat Q, aircraft speed $v_E = V$, bypass ratio $\mu = \dot{m}_B/\dot{m}_L = 3.17$, effective exit cross sections $A_C = 0.125$ m² and $A_B = 0.252$ m², and EGT. The indicated EGT is used to control the temperature at the entrance to the high-pressure turbine based on measured temperatures after the low-pressure turbine. Therefore the indicated value is an engine-specific empirical function of the total temperature $T_t = h_t/c_p$ at core and bypass exits, EGT $= kT_{tC} + \min\{40, 73 - T_{tB}\}$, with $k \cong 0.886$ (all temperatures in °C) for the presently used engine version. The air/fuel mass flow ratio is AFR $= \dot{m}_L/\dot{m}_F$. The propulsion efficiency $\eta = (FV + gwM/2)/(\dot{m}_F Q)$ includes the (small) contribution from potential energy gain during climb. Table 4 lists the results of this analysis.

The emission index for soot may be estimated from data on the smoke number SN. The SN is the percentage change in reflectance of a stained filter after passage of a given volume exhaust sample [*Champagne*, 1971]. The International Civil Aviation Organization, Montreal(ICAO) emissions database lists the present engine with SN = 2.7, 10.9, 38.4, and 46.3, for 7, 30, 85, and 100% takeoff thrust, with 0.053, 0.146, 0.416, and 0.498 kg s⁻¹ fuel flow, respectively. From the given ICAO smoke number values SN, we compute the soot particle concentration c_{soot} (mass per standard exhaust volume) at the core engine exit using relationships as given by *Champagne* [1971] and *Hurley* [1993]. The emission index is determined from $EI_{soot} = c_{soot} A_C v_C T_C/(\dot{m}_F T_0)$, for surface pressure and reference temperature $T_0 = 273$ K. Jet engine exit velocities v_C and temperatures T_C were taken from performance calculations provided by the engine manufacturer. The resultant emission indices are 0.01, 0.45, 2, and 3, for 7, 30, 85, and 100% takeoff thrust, respectively. In order to estimate EI_{soot} in flight one needs to know the relationship between soot emission and the engine parameters. Assuming the same emission for the same fuel flow rate leads to an estimate of about $EI_{soot} \cong 0.5$ g kg⁻¹.

Appendix 3: Estimates of Coagulation Timescales

For particles smaller than 1 μm, coagulation is mainly due to Brownian motion [*Pruppacher and Klett*, 1980, pp. 366-379]. For rough estimates, we assume monodispersed particles and that all soot and sulfuric acid is distributed initially on particles of equal diameter d within the young plume $(D = 2$ m, age < 0.3 s) or in the aged plume $(D = 20$ m, age < 30 s). The timescales for mutual coagulation of soot particles and H_2SO_4/H_2O droplets and for coagulation of such droplets on soot particles of 60 nm diameter are computed using equations 12-44 and 12-37 of *Pruppacher and Klett* [1980]. Table 7 lists the results for $D = 2$ m and various sulfur contents. The coagulation time depends on the particle number density, $t \sim N^{-1} \sim d^3 D^2/EI$, and is 100 times longer for $D = 20$ m, therefore. The coagulation times are very short for small initial particle diameters. The results show that the soot if consisting initially of particles less than 7 nm diameter would have coagulated quickly in the young plume, whereas soot particles with median diameter above 20 nm survive the aged plume. Sulfuric acid particles coagulate quickly in

Table 7. Computed Coagulation Times

		t_{acid}			
d	t_{soot}	$S = 5500$	$S = 170$	$S = 2$	$t_{acid/soot}$
1	4×10^{-5}	2×10^{-4}	0.008	0.6	0.2
7	0.1	0.6	18	1500	10
60	500	3000	~ day	~ days	200

Particle diameter d in nanometers and fuel sulfur content S in ppm. Coagulation times in seconds for a plume diameter of 2 m: t_{soot} for soot particles, t_{acid} for H_2SO_4/H_2O droplets, $t_{acid/soot}$ for acid droplets and 60 nm diameter soot particles.

the young plume if smaller than 1 nm on average either with each other or with the larger soot particles. Sulfuric acid particles with average diameter of 7 nm partly coagulate with each other and with the soot particles. Coagulation of sulfuric acid particles is much quicker for high sulfur emissions, but may be still important for 2 ppm sulfur fuel content. Note that the computations assumed very quick conversion of 0.4% of the SO_2 into H_2SO_4, quick nucleation, and sticking of all acid particles on soot. More complete model simulations are required to assess the details of particle formation.

Notation

a fraction of soot particles forming condensation nuclei.
c_p specific heat capacity at constant pressure.
d particle diameter.
D plume diameter.
EI emission index.
F thrust per engine.
g gravity.
m water vapor mass fraction.
m_{LM} maximum water vapor mass fraction available for condensation.
$\dot{m}_F$ fuel flow rate.
M, M_i mass of aircraft, molar mass of species i.
N number density: particles per volume.
p pressure.
Q combustion heat per fuel mass.
R_i gas constant of species i.
s $[H_2SO_4] / [SO_2]$ conversion fraction.
S sulfur mass fraction in fuel.
T_E environmental temperature.
T_{LC} threshold temperature: liquid contrails may form for $T_E < T_{LC}$.
u, v, w velocity components.
V true air speed of aircraft.
η $FV/(\dot{m}_F Q)$ overall propulsion efficiency.
ρ density.
τ optical thickness.
$[i]$ mixing ratio of species i.

References

American Society for Testing and Materials (ASTM), Standard specification for aviation fuels, D 1655-93a, in *Annual Book of ASTM Standards, 05.01*, Philadelphia, Pa., pp. 555-563, 1994.

Appleman, H., The formation of exhaust condensation trails by jet aircraft, *Bull. Am. Meteorol. Soc., 34*, 14-20, 1953.

Arnold, F., R. Fabian, and W. Joos, Measurements of the height variation of sulfuric acid vapor-concentrations in the stratosphere, *Geophys. Res. Lett., 8*, 293-296, 1981.

Arnold, F., J. Schneider, M. Klemm, J. Scheid, T. Stilp, H. Schlager, P. Schulte, and M. E. Reinhardt, Mass spectrometric measurements of SO₂ and reactive nitrogen gases in exhaust of commercial jet airliners at cruise altitude, *Rep. DLR Mitt. 94-06*, pp. 323-328, Dtsch. Forsch. für Luft- und Raumfahrt, Köln, 1994.

Baumgardner, D., and W. A. Cooper, Airborne measurements in jet contrails: Characterization of the microphysical properties of aircraft wakes and exhausts, *Rep. DLR Mitt. 94-06*, pp. 418-423, Dtsch. Forsch. für Luft- und Raumfahrt, Köln, 1994.

Bögel, W., and R. Baumann, Test and calibration of the DLR Falcon wind measuring system by maneuvers, *J. Atmos. Oceanic Technol., 8*, 5-18, 1991.

Busen, R., and U. Schumann, Visible contrail formation from fuels with different sulfur contents, *Geophys. Res. Lett., 22*, 1357-1360, 1995.

Carslaw, K. S., S. L. Clegg, and P. Brimblecombe, A thermodynamic model of the system HCl–HNO₃–H₂SO₄–H₂O, including solubilities of HBr, from <200 to 328 K, *J. Phys. Chem., 99*, 11557-11574, 1995.

Champagne, D. L., Standard measurement of aircraft gas turbine engine exhaust smoke, *Rep. ASME 71-GT-88*, Am. Soc. Mech. Eng., New York, 1971.

Chylek, P., and J. Hallett, Enhanced absorption of solar radiation by cloud droplets containing soot particles in their surface. *Q. J. R. Meteorol. Soc., 118*, 167-172, 1992.

Chylek, P., V. Ramaswamy, and R. J. Cheng, Effect of graphitic carbon on the albedo of clouds, *J. Atmos. Sci., 41*, 3076-3084, 1984.

DeMott, P. J., An exploratory study of ice nucleation by soot aerosols, *J. Appl. Meteorol., 29*, 1072-1079, 1990.

Dye, J. E., and D. Baumgardner, Evaluation of the forward scattering spectrometer probe, I, Electronic and optical studies, *J. Oceanic Atmos. Technol., 1*, 329-344, 1984.

Fahey, D. W., et al., In situ observations in aircraft exhaust plumes in the lower stratosphere at mid-latitudes, *J. Geophys. Res., 100*, 3065-3074, 1995.

Frenzel, A., and F. Arnold, Sulfuric acid cluster ion formation by jet engines: Implications for sulfuric acid formation and nucleation, *Rep. DLR Mitt. 94-06*, pp. 106-112, Dtsch. Forsch. für Luft- und Raumfahrt, Köln, 1994.

Gayet, J.-F., G. Febvre, G. Brogniez, H. Chepfer, W. Renger, and P. Wendling, Microphysical and optical properties of cirrus and contrails: Cloud field study on 13 October 1989, *J. Atmos. Sci., 53*, 126-138, 1996.

Hagen, D. E., M. B. Trueblood, and P. D. Whitefield, A field sampling of jet exhaust aerosols, *Particulate Sci. Technol., 10*, 53-63, 1992.

Hallett, J., J. G. Hudson, and C. F. Rogers, Characterization of combustion aerosols for haze and cloud formation, *Aerosol Sci. Technol., 10*, 70-83, 1990.

Hamill, P., R. B. Turco, C. S. Kiang, O. B. Toon, and R. C. Whitten, An analysis of various nucleation mechanisms for sulfate particles in the stratosphere, *J. Aerosol Sci., 13*, 561-585, 1982.

Haynes, B. S., and H. G. Wagner, Soot formation, *Prog. Energy Combust. Sci., 7*, 229-273, 1981.

Heymsfield, A. J., and R. M. Sabin, Cirrus crystal nucleation by homogeneous freezing of solution droplets, *J. Atmos. Sci., 46*, 2252-2264, 1989.

Hofmann, D. J., Aircraft sulfur emissions, *Nature, 349*, 659-660, 1991.

Hofmann, D. J., and J. M. Rosen, Balloon observations of a particle layer injected by a stratospheric aircraft at 23 km, *Geophys. Res. Lett., 5*, 511-514, 1978.

Hurley, C. D., Smoke measurements inside a gas turbine combustor, paper AIAA 93-2070 presented at AIAA 29th Joint Propulsion Conference, Am. Inst. Aeron. and Astron., Monterey, Calif., June 28-30, 1993.

JANE, *Jane's all the World's Aircraft*, edited J. W. R. Taylor, Paulton House, London, 1975.

JANE, *Jane's all the World's Aircraft*, edited J. W. R. Taylor, Paulton House, London, 1976.

JANE, *Jane's all the World's Aircraft*, edited J. W. R. Taylor, Paulton House, London, 1980.

Kärcher, B., Transport of exhaust products in the near trail of a jet engine under atmospheric conditions, *J. Geophys. Res., 99*, 14509-14517, 1994.

Kärcher, B., T. Peter, and R. Ottmann, Contrail formation: Homogeneous nucleation of H₂SO₄/H₂O droplets, *Geophys. Res. Lett., 22*, 1501-1504, 1995.

Knollenberg, R. G., Measurements of the growth of the ice budget in a persisting contrail, *J. Atmos. Sci., 29*, 1367-1374, 1972.

Lammel, G., and T. Novakov, Water nucleation properties of carbon black and diesel soot particles, *Atmos. Environ., 29*, 813-823, 1995.

Mertes, S., F. Schröder, and A. Wiedensohler, The particle detection efficiency curve of the TSI 3010 CPC as a function of the temperature difference between saturator and condensor, *Aerosol Sci. Technol., 23*, 257-261, 1995.

Miake-Lye, R. C., M. Martinez-Sanchez, R. C. Brown, and C. E. Kolb, Plume and wake dynamics, mixing, and chemistry behind a high speed civil transport aircraft, *J. Aircr., 30*, 467-479, 1993.

Miake-Lye, R.C., R. C. Brown, M. R. Anderson, and C. E. Kolb, Calculations of condensation and chemistry in an aircraft contrail, *Rep. DLR Mitt. 94-06*, pp. 274-279, Dtsch. Forsch. für Luft- und Raumfahrt, Köln, 1994.

Mirabel, P., and J. L. Katz, Binary homogeneous nucleation as a mechanism for the formation of aerosols, *J. Chem. Phys., 60*, 1138-1144, 1974.

Möhler, O., and F. Arnold, Gaseous sulfuric acid and sulfur dioxide measurements in the arctic troposphere and lower stratosphere: Implications for hydroxyl radical abundances, *Geophys. Res. Lett., 19*, 1763-1766, 1992.

Noone, K. J., and H.-C. Hansson, Calibration of the TSI-3760 condensation nucleus counter for nonstandard operating conditions, *Aerosol Sci. Tech., 13*, 478-485, 1990.

Palmer, K. F., and D. Williams, Optical constants of sulfuric acid; application to the clouds of Venus?, *Appl. Opt., 14*, 208-219, 1975.

Parungo, F., B. Kopcewicz, C. Nagamoto, R. Schnell, P. Sheridan, C. Zhu, and J. Harris, Aerosol particles in the Kuwait oil fire plumes: Their morphology, size distribution, chemical composition, transport, and potential effect on climate, *J. Geophys. Res., 97*, 15867-15882, 1992.

Pitchford, M., J. G. Hudson, and J. Hallett, Size and critical supersaturation for condensation of jet engine exhaust particles, *J. Geophys. Res., 96*, 20787-20793, 1991.

Pruppacher, H. R., and J. D. Klett, *Microphysics of Clouds and Precipitation*, 714 pp., D. Reidel, Norwell, Mass., 1980.

Reiner, T., and F. Arnold, Laboratory flow reactor measurements of the reaction SO₃+H₂O+M -> H₂SO₄+M: Implications for gaseous H₂SO₄ and aerosol formation in the plumes of jet aircraft, *Geophys. Res. Lett., 20*, 2659-2662, 1993.

Sausen, R., and I. Köhler, Simulating the global transport of nitrogen oxides emissions from aircraft, *Ann. Geophys., 12*, 394-402, 1994.

Schmidt, E., Die Entstehung von Eisnebel aus den Auspuffgasen von Flugmotoren, in *Schriften der Deutschen Akademie der Luftfahrtforschung*, no. 44, pp. 1-22, R. Oldenbourg, München, 1941.

Schumann, U., On the effect of emissions from aircraft engines on the state of the atmosphere, *Ann. Geophys., 12*, 365-384, 1994.

Schumann, U., On conditions for contrail formation from aircraft exhausts, *Meteorol. Z., N. F. 5*, 3-22, 1996.

Schumann, U., P. Konopka, R. Baumann, R. Busen, T. Gerz, H. Schlager, P. Schulte, and H. Volkert, Estimate of diffusion parameters of aircraft exhaust plumes near the tropopause from nitric oxide and turbulence measurements, *J. Geophys. Res., 100*, 14147-14162, 1995.

Ström, J., R. Busen, M. Quante, B. Guillemet, P. R. A. Brown, and J.

Heintzenberg, Pre-EUCREX intercomparison of airborne humidity measuring instruments. *J. Atmos. Oceanic Technol.*, *11*, 1392-1399, 1994.

Turco, R. P., O. B. Toon, J. B. Pollack, R. C. Whitten, I. G. Poppoff, and P. Hamill, Stratospheric aerosol modification by supersonic transport and space shuttle operations - climate implications, *J. Appl. Meteorol.*, *19*, 78-89, 1980.

Turco, R. P., R. C. Whitten, and O. B. Toon, Stratospheric aerosols: Observation and theory, *Rev. Geophys.*, *20*, 233-279, 1982.

U.S. Environmental Protection Agency (EPA), *Compilation of Air Pollutant Emission Factors*, Vol. 2, *Mobile Sources*, 4th ed., PB87-205266, Ann Arbor, Mich., 1985.

Van de Hulst, H. C., *Light Scattering by Small Particles*, John Wiley, New York, 1957.

Wagner, P. E., Aerosol growth by condensation, in *Aerosol Microphysics II*, edited by W. H. Marlow, pp. 129-178, Springer-Verlag, New York, 1982.

World Meteorological Organization (WMO), Scientific Assessment of Ozone Depletion: 1994, Global Ozone Research and Monitoring Project, Rep. 37, Geneva, 1995.

Wyslouzil, B. E., K. L. Carleton, D. M. Sonnenfroh, W. T. Rawlins, and S. Arnold, Observation of hydration of single, modified carbon aerosols, *Geophys. Res. Lett.*, *21*, 2107-2110, 1994.

Zhang, Z., and B. Y. H. Liu, Performance of TSI 3760 condensation nuclei counter at reduced pressures and flow rates, *Aerosol Sci. Technol.*, *15*, 228-238, 1991.

Zhao, J., and R. P. Turco, Nucleation simulation in the wake of a jet aircraft in stratospheric flight, *J. Aerosol Sci.*, *26*, 779-795, 1995.

R. Baumann, R. Busen, K. Gierens, M. Krautstrunk, U. Schumann, and J. Stingl, Deutsche Forschungsanstalt für Luft- und Raumfahrt (DLR), Institut für Physik der Atmosphäre, Oberpfaffenhofen, Postfach 1116, D-82230 Wessling, Germany. (e-mail: Ulrich.Schumann@dlr.de)

F. P. Schröder and J. Ström, Stockholms Universitet, Meteorologiska Institutionen, S-10691 Stockholm, Sweden.